

# SN 2015an: a normal luminosity type II supernova with low expansion velocity at early phases

Raya Dastidar<sup>1,2\*</sup>, Kuntal Misra<sup>1,3</sup>, Stefano Valenti<sup>3</sup>, Jamison Burke<sup>4,5</sup>, Griffin Hosseinzadeh<sup>6</sup>, Anjasha Gangopadhyay<sup>1,7</sup>, D. Andrew Howell<sup>4,5</sup>, Mridweeka Singh<sup>1,7</sup>, Iair Arcavi<sup>8</sup>, Brijesh Kumar<sup>1</sup>, Curtis McCully<sup>4,5</sup>, Pankaj Sanwal<sup>1,7</sup> and S. B. Pandey<sup>1</sup>

<sup>1</sup>*Aryabhata Research Institute of observational sciencES, Manora Peak, Nainital 263 001 India*

<sup>2</sup>*Department of Physics & Astrophysics, University of Delhi, Delhi-110 007*

<sup>3</sup>*Department of Physics, University of California, 1 Shields Ave, Davis, CA 95616-5270, USA*

<sup>4</sup>*Las Cumbres Observatory, 6740 Cortona Dr., Suite 102, Goleta, CA 93117-5575, USA*

<sup>5</sup>*Department of Physics, University of California, Santa Barbara, CA 93106-9530, USA*

<sup>6</sup>*Center for Astrophysics | Harvard & Smithsonian, 60 Garden Street, Cambridge, MA 02138-1516, USA*

<sup>7</sup>*Pt.Ravi Shankar Shukla University, Raipur 492 010, India*

<sup>8</sup>*The School of Physics and Astronomy, Tel Aviv University, Tel Aviv 69978, Israel*

Accepted XXX. Received YYY; in original form ZZZ

## ABSTRACT

We present the photometry and spectroscopy of SN 2015an, a Type II Supernova (SN) in IC 2367. The recombination phase of the SN lasts up to  $\sim 120$  d, with a decline rate of 1.24 mag/100d, higher than the typical SNe IIP. The SN exhibits bluer colours than most SNe II, indicating higher ejecta temperatures. The absolute *V*-band magnitude of SN 2015an at 50 d is  $-16.83 \pm 0.04$  mag, pretty typical for SNe II. However, the  $^{56}\text{Ni}$  mass yield, estimated from the tail *V*-band light curve to be  $0.021 \pm 0.010 M_{\odot}$ , is comparatively low. The spectral properties of SN 2015an are atypical, with low  $H\alpha$  expansion velocity and presence of high velocity component of  $H\alpha$  at early phases. Moreover, the continuum exhibits excess blue flux up to  $\sim 50$  d, which is interpreted as a progenitor metallicity effect. The high velocity feature indicates ejecta-circumstellar material interaction at early phases. The semi-analytical modelling of the bolometric light curve yields a total ejected mass of  $\sim 12 M_{\odot}$ , a pre-supernova radius of  $\sim 388 R_{\odot}$  and explosion energy of  $\sim 1.8$  foe.

**Key words:** techniques: photometric – techniques: spectroscopic – supernovae: general – supernovae: individual: SN 2015an – galaxies: individual: IC 2367

## 1 INTRODUCTION

The hydrogen-dominant class of supernovae (SNe) designated as SNe II, are the fate of the majority of massive stars ( $\gtrsim 8 M_{\odot}$ ) which ensue from the gravitational collapse of the iron core in the red supergiant (RSG) stage (Smartt et al. 2009; Smartt 2015). SNe II are characterized by the presence of Balmer lines in their early spectra (Minkowski 1941), and those with abundant hydrogen either exhibit a plateau (P) or a linearly declining phase (L) in their light curve which lasts for about 100 days, before plummeting into the radioactive tail phase (Barbon et al. 1979). Three other subtypes exist: Type IIn, IIb and the 1987A-like, but hereafter we will mainly discuss SNe IIP and IIL conjointly

as SNe II. Direct evidence for RSG as progenitor of SNe II are proclaimed from fortuitous detection of the progenitor in pre-explosion images, which corroborated with the theoretical predictions of Grassberg et al. (1971); Chevalier (1976); Falk & Arnett (1977). The initial mass range, however, is constrained between 7-18  $M_{\odot}$  from the pre-explosion images, that raised the ‘RSG problem’ (Smartt et al. 2009; Smartt 2015), as RSGs more massive than 18  $M_{\odot}$  are known to exist observationally. This is further substantiated by the higher progenitor mass yields from hydrodynamical modelling of the SN observables (e.g. Pumo et al. 2017; Dastidar et al. 2018 and references therein). But ejecta masses of SNe II estimated from hydrodynamical modelling of light curve may not be robust and unique, as indicated in recent simulation of SNe II explosions by Dessart & Hillier (2019).

\* E-mail: rayadastidar@aries.res.in, rdastidr@gmail.com

The remarkable feature of the SNe II population is the

continuity in diversity. Despite the prominent dispersion in the observed properties of SNe II, which is apparent from the range of peak magnitudes ( $-14 \gtrsim M_B \gtrsim -18$ ; Patat et al. 1994), plateau luminosities ( $-15 > M_V > -18$ ; Hamuy 2003) and ejecta velocities ( $1500 < v_{ph}^{50} < 9600 \text{ km s}^{-1}$ ; Gutiérrez et al. 2017a), a continuum in the properties has been noted (Anderson et al. 2014b; Sanders et al. 2015). The progenitor and explosion properties, such as the radius of the progenitor, the mass of hydrogen envelope and the synthesized  $^{56}\text{Ni}$  mass, most likely gives rise to the continuity. External factors, such as the presence of a dense circumstellar (CS) shell in proximity to the progenitor star at the time of explosion could also be responsible for the observed continuum in the properties of SNe II (Morozova et al. 2017).

The spectra of SNe II exhibits broad P Cygni lines, which seems to disfavour the possibility of a major contribution of circumstellar interaction (CSI) of ejecta in powering these explosions, unlike SNe IIn, which are characterised by narrow emission lines of hydrogen. However, the interaction in SNe II can be hidden below the photosphere, and not be seen in narrow lines (e.g. iPTF14hls, Andrews & Smith 2018), and still contribute to the luminosity. A contribution of interaction to the luminosity, with spectra bereft of narrow lines, is also possible for certain shallow wind density profiles (Moriya & Tominaga 2012). The spectra of low-luminosity ( $-14 > M_V^{max} > -15.5$ ) class of SNe II (e.g. SN 2005cs) exhibit weak absorption features superimposed on a dominant blue continuum lasting up to  $\lesssim 30$  d post explosion (Spiro et al. 2014), owing to the underenergetic nature of the explosion. However, normal luminosity SNe showing weak absorption component (e.g. LSQ13fn, Polshaw et al. 2016) are most likely the terminal explosion of a sub-solar metallicity progenitor (Dessart et al. 2013).

Despite the surge in the number of studies undertaken for individual as well as samples of SNe II, a number of issues remain inconclusive, such as the source of the observed diversity in their photometric and spectroscopic properties. Dust formation at late times and CSM forged in the latest stages of the evolution can considerably tweak the observed properties of the explosion. To enrich our understanding of the inhomogeneous class of SNe II, detailed studies of these events particularly the deviant objects are important.

In this paper, we present the photometric and spectroscopic analysis of a Type II SN, SN 2015an, discovered by Berto Monard (Bronberg Observatory) in the galaxy IC 2367 on 2015 September 13.15 UT (JD 2457278.65) at an unfiltered magnitude of 15.2 mag. The classification spectrum was procured by the Las Cumbres Observatory (LCO) Supernova Key Project on 2015 September 26.7 UT (Hosseinzadeh et al. 2015), nearly two weeks from discovery, with the robotic FLOYDS instrument mounted on the Faulkes Telescope South (FTS). The spectrum exhibited a striking blue continuum and a significantly low H $\alpha$  expansion velocity ( $\sim 5000 \text{ km s}^{-1}$ ). The predominance of blue continuum in spectra up to two weeks past discovery is generally observed in low-luminosity SNe, however, the expansion velocity of H $\alpha$  and the luminosity of SN 2015an are comparatively higher than the low-luminosity events (see Figs. 3 & 8). This led to its classification as a peculiar SN II. The details of SN 2015an and its host galaxy IC 2367 are given in Table 1.

The Virgo infall distance to the galaxy IC 2367 is  $30.7 \pm 0.7$  Mpc, where we have used the recessional ve-

**Table 1.** Basic information on SN 2015an and the host galaxy IC 2367. The host galaxy parameters are taken from NED.

Host galaxy	IC 2367
Galaxy type	SBb
Redshift	$0.00817 \pm 0.00001^\dagger$
Major Diameter	2.4 arcmin
Minor Diameter	1.7 arcmin
Helio. Radial Velocity	$2488 \pm 3 \text{ km s}^{-1}$
Offset from nucleus	$71''.0 \text{ E}, 4''.0 \text{ N}$
Distance	$30.5 \pm 0.6 \text{ Mpc}^{\dagger\dagger}$
Total Extinction E(B-V)	$0.0875 \pm 0.0012 \text{ mag}^{\dagger\dagger}$
SN type	II
Date of Discovery	2457278.65 (JD)
Estimated date of explosion	$2457268.5 \pm 1.6$ (JD) $^{\dagger\dagger}$

$^\dagger$  Theureau et al. (1998)  $^{\dagger\dagger}$  This paper.

locity of the galaxy  $v_{Vir} = 2259 \pm 3 \text{ km s}^{-1}$  from HyperLeda (Makarov et al. 2014) and Hubble constant  $H_0 = 73.48 \pm 1.66 \text{ km s}^{-1} \text{ Mpc}^{-1}$  (Riess et al. 2018). We used the expanding photosphere method (EPM) to estimate the distance to SN 2015an (details in Sect. 5), which yielded  $29.8 \pm 1.5 \text{ Mpc}$ . The weighted mean of the two estimations is  $30.5 \pm 0.6 \text{ Mpc}$ , which we have adopted as distance to SN 2015an in this paper. EPM also estimates the explosion epoch to be  $2457268.5 \pm 1.6 \text{ d}$  (2015 September 03 UT) which we will refer to as 0 d.

The Galactic reddening  $E(B-V)_{MW}$  in the line of sight of IC 2367 is  $0.0875 \pm 0.0012 \text{ mag}$ , obtained from the extinction dust maps of Schlafly & Finkbeiner (2011). In our best resolution optical spectra, we do not detect the absorption features due to interstellar Na I D lines from the Galaxy. From a set of best SNR spectra, we constructed a composite spectrum following the prescription in Gall et al. (2015) to determine the limiting equivalent width (EW) of Na I D absorption feature at the redshift of the host galaxy. Gaussian profile of varying EWs were fitted to the Na I D absorption line in the stacked spectrum and plausibly a weak Na I D line with EW of 0.2 Å could be discerned. This corresponds to a host galaxy reddening of  $< 0.02 \text{ mag}$  (using eqn (9) of Poznanski et al. 2012). The weak Na I D feature indicates negligible reddening contribution from the host, which is in agreement with the remote location of the SN from the main body of its host galaxy. Consequently, we infer that the total reddening is arising only from the Galactic component, that is  $E(B-V)_{tot} = 0.0875 \pm 0.0012 \text{ mag}$  and is used in the rest of our analysis.

The paper is structured as follows. Sect. 2 gives details of the data and reduction procedure. We investigate the photometric and spectroscopic properties of SN 2015an in Sect. 3 and Sect. 4, respectively. The distance derived using the expanding photosphere method is elaborated in Sect. 5. The modelling of the bolometric light curve using semi-analytic methods is discussed in Sect. 6. Finally, we examine the overall properties of SN 2015an in Sect. 7 and present a short summary of the paper in Sect. 8.

## 2 SN 2015AN: PHOTOMETRY AND SPECTROSCOPY

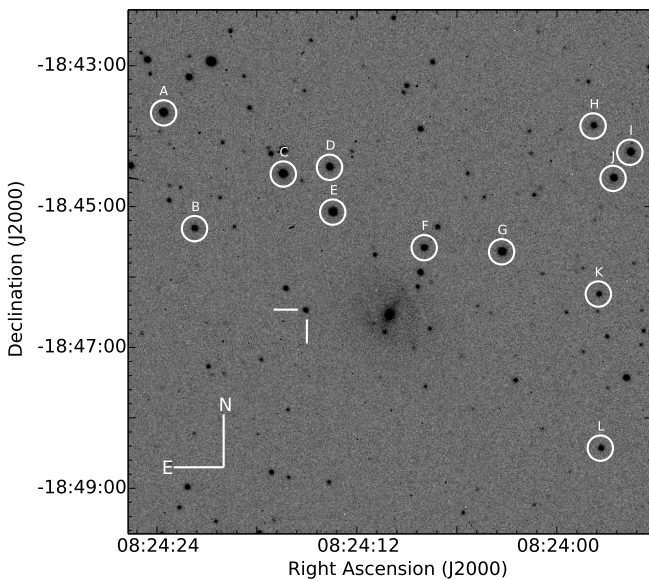
The photometric campaign of SN 2015an was triggered on the day of its discovery using instruments equipped with

**Table 2.** Summary of the instruments used for the observational campaign of SN 2015an.

Telescope	Location	Instrument	Pixel Scale ("'/pixel)	Imaging bands	Dispersers/ Grisms	
1.04m Sampurnanand Telescope (ST)	ARIES Observatory, India	Tek 1k×1k	0.53	<i>VRI</i>	-	1
1.3m Devasthal Fast Optical Telescope (DFOT)	ARIES Observatory, India	Andor 512×512	0.64	<i>BVRI</i>	-	2
1m LCO	Siding Spring Observatory	Sinistro	0.389	<i>BVg'r'i'</i>	-	3
1m LCO	South African Astronomical Observatory	Sinistro	0.389	<i>BVg'r'i'</i>	-	4
1m LCO	Cerro Tololo Interamerican Observatory	Sinistro	0.389	<i>BVg'r'i'</i>	-	5
1m LCO	McDonald Observatory, USA	Sinistro	0.389	<i>BVg'r'i'</i>	-	6
2m FTN	Halekala Observatory, USA	Spectral, FLOYDS	0.304, 0.34	<i>g'r'i'</i>	Cross disperser	7
2m FTS	Siding Spring Observatory, Australia	FLOYDS	0.34	-	Cross disperser	8

**Table 3.** Coordinates and photometry of the local sequence reference stars in the *BVg'r'i'* bands.

ID	$\alpha_{J2000.0}$ (hh:mm:ss)	$\delta_{J2000.0}$ (dd:mm:ss)	<i>B</i> mag	<i>V</i> mag	<i>g'</i> mag	<i>r'</i> mag	<i>i'</i> mag
A	08:24:23.6	-18:43:40.2	14.227 (.015)	13.729 (.021)	13.928 (.032)	13.594 (.019)	13.503 (.014)
B	08:24:21.7	-18:44:26.6	15.428 (.028)	14.866 (.037)	15.095 (.027)	14.717 (.024)	14.580 (.033)
C	08:24:16.4	-18:45:18.8	14.752 (.029)	13.458 (.024)	14.056 (.033)	12.999 (.023)	12.574 (.015)
D	08:24:13.6	-18:43:54.4	14.926 (.027)	14.334 (.009)	14.588 (.035)	14.184 (.016)	14.017 (.046)
E	08:24:13.4	-18:45:04.7	14.220 (.025)	13.553 (.018)	13.827 (.034)	13.347 (.024)	13.174 (.018)
F	08:24:07.9	-18:45:35.1	15.489 (.040)	14.613 (.025)	14.996 (.036)	14.295 (.019)	14.035 (.047)
G	08:24:03.3	-18:47:24.2	14.724 (.022)	13.749 (.015)	14.194 (.034)	13.446 (.015)	13.129 (.026)
H	08:23:57.8	-18:43:51.3	15.516 (.052)	15.071 (.026)	15.233 (.038)	14.936 (.010)	14.927 (.038)
I	08:23:55.6	-18:44:13.7	14.946 (.034)	14.086 (.018)	14.474 (.035)	13.832 (.016)	13.592 (.016)
J	08:23:56.6	-18:44:35.9	14.492 (.033)	14.330 (.022)	14.332 (.039)	14.381 (.028)	14.543 (.028)
K	08:23:57.5	-18:46:14.5	16.709 (.054)	15.575 (.031)	16.122 (.038)	15.089 (.041)	14.759 (.047)
L	08:27:57.4	-18:48:25.8	16.138 (.031)	15.31 (.016)	15.680 (.042)	15.039 (.030)	14.840 (.044)

**Figure 1.** SN 2015an in IC 2367, star ID for local standards have been marked.

broadband *BVRI* and *g'r'i'z'* filters as listed in Table 2. The photometric observations continued up to 261 d from explosion. The pre-processing of the images including bias

and flat-field corrections were carried out in IRAF<sup>1</sup> environment and cosmic rays were cleaned using the L.A.COSMIC routine (van Dokkum 2001). Owing to the remoteness of SN 2015an from its host galaxy nucleus (at a deprojected radial distance of 13.9 kpc), we performed the point spread function photometry using DAOPHOT II (Stetson 1987) to derive the instrumental magnitudes. The LCO photometry was carried using *lcogtspipe* designed by Stefano Valenti (see details in Valenti et al. 2016). The instrumental magnitudes were calibrated using the standard magnitudes of 12 local standard stars in the SN field obtained from the AAVSO Photometric All-Sky Survey (APASS<sup>2</sup>) catalog. The local standards are marked in Fig. 1 and their magnitudes are listed in Table 3. The calibrated SN magnitudes, thus obtained, are listed in Table 4.

The spectroscopic observations of SN 2015an commenced with the acquisition of the classification spectrum, followed by 18 epochs of observations (observation log in Table 5) up to 158 d from explosion with the LCO telescopes. The FLOYDS spectrograph at the Faulkes Telescope North and South (FTN and FTS) gives a wavelength coverage of

<sup>1</sup> IRAF stands for Image Reduction and Analysis Facility distributed by the National Optical Astronomy Observatories which is operated by the Association of Universities for research in Astronomy, Inc., under cooperative agreement with the National Science Foundation.

<sup>2</sup> <https://www.aavso.org/apass>

**Table 4.** Optical photometry of SN 2015an.

UT Date (yyyy-mm-dd)	JD 2457000+	Phase <sup>†</sup> (days)	<i>B</i> (mag)	<i>V</i> (mag)	<i>g'</i> (mag)	<i>r'</i> (mag)	<i>i'</i> (mag)	<i>Tel</i>
2015-09-13.8	279.3	10.8	-	-	-	15.56 ± 0.02	15.75 ± 0.01	3
2015-09-14.1	279.6	11.1	-	-	15.37 ± 0.01	15.63 ± 0.02	15.78 ± 0.02	4
2015-09-15.8	281.3	12.8	15.59 ± 0.01	15.52 ± 0.01	-	-	-	3
2015-09-16.1	281.6	13.1	-	-	15.48 ± 0.01	15.63 ± 0.01	15.82 ± 0.02	4
2015-09-18.4	283.9	15.4	-	-	15.62 ± 0.01	15.65 ± 0.01	15.74 ± 0.01	5
2015-09-19.4	284.9	16.4	-	-	15.56 ± 0.08	15.60 ± 0.01	15.72 ± 0.01	5
2015-09-20.8	286.2	17.7	-	-	15.48 ± 0.10	15.58 ± 0.01	15.67 ± 0.01	3
2015-09-21.1	286.6	18.1	-	-	15.40 ± 0.01	15.54 ± 0.01	15.67 ± 0.01	4
2015-09-21.4	286.9	18.4	15.60 ± 0.01	15.47 ± 0.01	-	-	-	5
2015-09-22.4	287.9	19.4	15.64 ± 0.01	15.49 ± 0.01	-	15.54 ± 0.01	15.62 ± 0.01	5
2015-09-26.4	291.8	23.3	15.75 ± 0.02	15.56 ± 0.02	15.55 ± 0.01	15.57 ± 0.01	15.65 ± 0.02	5
2015-10-01.8	297.3	28.8	15.89 ± 0.01	15.58 ± 0.01	15.66 ± 0.01	15.52 ± 0.01	15.52 ± 0.01	3
2015-10-05.7	301.2	32.7	16.03 ± 0.01	15.66 ± 0.01	15.75 ± 0.01	15.57 ± 0.01	15.59 ± 0.01	3
2015-10-13.7	309.2	40.7	16.34 ± 0.02	15.77 ± 0.01	16.00 ± 0.01	15.64 ± 0.01	15.60 ± 0.02	5
2015-10-17.3	312.8	44.3	16.52 ± 0.02	15.87 ± 0.01	16.14 ± 0.01	15.75 ± 0.01	15.67 ± 0.02	6
2015-10-26.5	321.9	53.4	16.87 ± 0.02	16.06 ± 0.02	-	15.86 ± 0.01	-	4
2015-10-31.1	326.6	58.1	16.95 ± 0.03	16.12 ± 0.02	16.47 ± 0.02	15.92 ± 0.01	15.81 ± 0.02	4
2015-11-05.1	331.6	63.1	17.15 ± 0.04	16.18 ± 0.02	16.58 ± 0.02	15.99 ± 0.04	-	4
2015-11-09.1	335.6	67.1	-	16.24 ± 0.02	16.63 ± 0.01	16.03 ± 0.01	15.92 ± 0.02	4
2015-11-09.9	336.4	67.9	-	16.38 ± 0.01	-	15.94 ± 0.01	15.96 ± 0.01	1
2015-11-10.9	337.4	68.9	-	16.35 ± 0.01	-	16.02 ± 0.01	15.91 ± 0.01	1
2015-11-13.3	339.8	71.3	-	16.28 ± 0.02	-	16.02 ± 0.02	16.01 ± 0.04	5
2015-11-16.9	343.4	74.9	17.38 ± 0.04	16.28 ± 0.02	16.73 ± 0.02	16.03 ± 0.01	15.95 ± 0.02	4
2015-11-20.7	347.2	78.7	17.32 ± 0.04	16.31 ± 0.02	16.78 ± 0.02	16.04 ± 0.01	15.93 ± 0.02	3
2015-11-22.6	349.1	80.6	17.46 ± 0.04	16.34 ± 0.02	16.91 ± 0.02	16.10 ± 0.02	16.00 ± 0.02	3
2015-11-24.1	350.6	82.1	17.47 ± 0.04	16.41 ± 0.02	16.89 ± 0.02	16.12 ± 0.01	16.04 ± 0.02	4
2015-11-27.9	354.4	85.9	17.39 ± 0.05	16.49 ± 0.03	16.94 ± 0.02	16.18 ± 0.02	16.06 ± 0.02	4
2015-12-05.9	362.4	93.9	17.64 ± 0.03	16.60 ± 0.01	-	16.28 ± 0.01	16.15 ± 0.01	2
2015-12-06.9	363.4	94.9	-	16.64 ± 0.03	17.07 ± 0.02	16.24 ± 0.02	16.15 ± 0.03	4
2015-12-10.7	367.1	98.6	17.74 ± 0.03	16.59 ± 0.02	17.15 ± 0.02	16.34 ± 0.01	16.21 ± 0.02	3
2015-12-14.9	371.5	103.0	17.87 ± 0.05	16.74 ± 0.03	17.28 ± 0.02	16.42 ± 0.02	16.32 ± 0.02	4
2015-12-18.4	374.9	106.4	17.99 ± 0.04	16.84 ± 0.02	17.32 ± 0.02	16.46 ± 0.02	16.36 ± 0.02	6
2015-12-22.1	378.6	110.1	18.20 ± 0.07	16.96 ± 0.02	-	16.55 ± 0.02	16.44 ± 0.04	5
2015-12-23.9	380.4	111.9	-	17.22 ± 0.02	-	16.66 ± 0.01	16.57 ± 0.01	1
2015-12-25.8	382.4	113.9	-	-	-	-	16.54 ± 0.04	4
2015-12-29.6	386.1	117.6	18.43 ± 0.15	-	17.56 ± 0.03	-	-	3
2015-12-30.7	387.2	118.7	-	17.18 ± 0.02	-	16.68 ± 0.01	16.62 ± 0.01	1
2016-01-01.8	389.3	120.8	-	17.31 ± 0.02	-	16.90 ± 0.01	16.76 ± 0.01	1
2016-01-02.7	390.2	121.7	-	17.27 ± 0.01	-	16.80 ± 0.01	16.75 ± 0.01	1
2016-01-02.9	390.4	121.9	18.70 ± 0.10	17.26 ± 0.05	-	-	16.64 ± 0.03	4
2016-01-03.8	391.3	122.8	-	-	-	16.85 ± 0.01	16.79 ± 0.01	1
2016-01-05.7	393.2	124.7	-	17.42 ± 0.01	-	16.92 ± 0.01	16.87 ± 0.01	1
2016-01-08.1	395.6	127.1	18.93 ± 0.10	17.65 ± 0.04	18.38 ± 0.04	17.10 ± 0.03	17.07 ± 0.04	5
2016-01-11.5	399.0	130.5	19.56 ± 0.12	18.31 ± 0.06	19.06 ± 0.10	17.74 ± 0.04	17.64 ± 0.06	3
2016-01-12.7	400.2	131.7	19.94 ± 0.04	18.64 ± 0.01	-	18.16 ± 0.02	17.97 ± 0.02	2
2016-01-13.7	401.2	132.7	20.17 ± 0.06	19.01 ± 0.02	-	18.16 ± 0.01	18.14 ± 0.01	2
2016-01-15.8	403.3	134.8	20.41 ± 0.06	19.34 ± 0.02	-	18.50 ± 0.01	18.13 ± 0.01	2
2016-01-16.8	404.2	135.7	20.49 ± 0.12	19.40 ± 0.06	-	18.53 ± 0.02	18.31 ± 0.02	2
2016-01-20.2	407.7	139.2	-	19.68 ± 0.01	20.13 ± 0.09	-	18.56 ± 0.10	5
2016-01-30.6	418.1	149.6	-	19.71 ± 0.05	-	18.98 ± 0.02	18.79 ± 0.03	2
2016-01-31.7	419.2	150.7	20.97 ± 0.16	19.60 ± 0.04	-	18.98 ± 0.02	18.90 ± 0.02	2
2016-02-03.8	422.3	153.8	20.86 ± 0.28	19.90 ± 0.08	20.34 ± 0.09	18.86 ± 0.03	18.76 ± 0.09	4
2016-02-08.2	426.7	158.2	21.12 ± 0.15	19.80 ± 0.05	20.44 ± 0.10	19.03 ± 0.05	19.00 ± 0.06	5
2016-02-10.7	429.2	160.7	-	-	-	18.92 ± 0.03	18.94 ± 0.04	1
2016-02-10.7	429.2	160.7	-	19.68 ± 0.03	-	18.80 ± 0.02	18.66 ± 0.02	2
2016-02-11.7	430.2	161.7	-	19.70 ± 0.06	-	18.94 ± 0.02	18.90 ± 0.04	2
2016-02-11.7	430.2	161.7	-	-	-	18.90 ± 0.03	18.97 ± 0.04	1
2016-02-12.7	431.2	162.7	21.12 ± 0.15	19.88 ± 0.05	-	19.00 ± 0.02	18.87 ± 0.03	2
2016-02-14.2	432.7	164.2	20.95 ± 0.02	19.86 ± 0.11	20.45 ± 0.15	19.14 ± 0.03	19.19 ± 0.05	5
2016-02-26.6	445.1	176.6	-	-	-	19.07 ± 0.02	19.04 ± 0.03	1
2016-02-27.7	446.2	177.7	-	-	-	19.10 ± 0.03	19.00 ± 0.02	1
2016-03-01.7	449.2	180.7	-	-	-	18.93 ± 0.02	18.99 ± 0.03	1
2016-03-02.7	450.2	181.7	-	-	-	19.02 ± 0.02	19.02 ± 0.03	1
2016-03-05.4	452.9	184.4	-	-	20.49 ± 0.03	18.99 ± 0.01	19.28 ± 0.03	7
2016-04-10.3	488.7	220.2	-	-	20.76 ± 0.04	-	19.71 ± 0.02	7
2016-05-20.9	529.5	261.0	-	-	20.98 ± 0.19	19.92 ± 0.07	20.76 ± 0.12	5

†since explosion epoch  $t_0 = \text{JD } 2457268.5$  (2015 September 03)

**Table 5.** Log of the spectroscopic observations.

UT Date	Phase <sup>†</sup> (Days)	Telescope
2015-09-26.7	23.8	FTS
2015-10-01.7	28.8	FTS
2015-10-03.7	30.8	FTS
2015-10-04.7	31.8	FTS
2015-10-06.7	33.6	FTS
2015-10-07.7	34.8	FTS
2015-10-15.6	42.6	FTN
2015-10-25.7	52.8	FTS
2015-11-02.5	60.6	FTN
2015-11-10.7	68.6	FTS
2015-11-22.7	80.8	FTS
2015-11-30.5	88.4	FTN
2016-12-08.5	96.4	FTN
2016-12-17.6	105.6	FTS
2016-12-25.6	113.6	FTS
2016-01-02.4	121.4	FTN
2016-01-11.5	130.6	FTN
2016-01-31.5	150.6	FTS
2016-02-08.4	158.4	FTS

<sup>†</sup>since explosion epoch  $t_0 = \text{JD } 2457268.5$  (2015 September 03)

3200-9000 Å with a resolution ranging from 400-700. The 1D wavelength and flux calibrated spectra extraction were carried out using the `floydsspec` pipeline<sup>3</sup>. The calibrated spectra were scaled with a factor derived by matching the photometric and spectroscopic continuum flux, thereby correcting for the slit losses. Finally the spectra were corrected for the heliocentric redshift of the host galaxy.

### 3 LIGHT CURVE ANALYSIS

The early light curve (LC) of SN 2015an rises to a peak in the  $r'$  and  $i'$  bands, while the bluer bands are in the early cooling phase as shown in the top panel of Fig 2. The peak of the redder bands are estimated following the procedure in González-Gaitán et al. (2015), where the peak is estimated by fitting a phenomenological function introduced by Bazin et al. (2009) to the LC (see eqn. 1 of the paper). The best fit of the functional form is shown in the inset of the top panel of Fig. 2. The rise to maximum from explosion in the  $r'$  and  $i'$  bands are  $16.6 \pm 3.7$  d and  $25.2 \pm 5.1$  d respectively. The multi-band LC changes slope around 55 d since explosion, when the  $Vr'i'$  LCs transits to the plateau phase, while  $Bg'$  LCs are in a relatively steeper declining phase. The plateau lasts for around 120 d, followed by a sharp fall in brightness after which the SN enters the exponentially declining phase powered by the emission from the decay of  $^{56}\text{Co} \rightarrow ^{56}\text{Fe}$ .

We performed a linear fit to the  $V$ -band light curve to estimate the initial steeper decline ( $s_1 = 0.78 \pm 0.02$  mag/50 d) and the second shallower decline ( $s_2 = 0.62 \pm 0.02$  mag/50 d) before the light curve falls off from the plateau. An overall decline rate,  $s_{50V}$  including both these regions (15 to 120 d) is also fitted. We used eqn 1 of Valenti et al. (2016) to derive other LC parameters such as the drop in magnitude from the plateau to the tail phase ( $a_0$ ), the

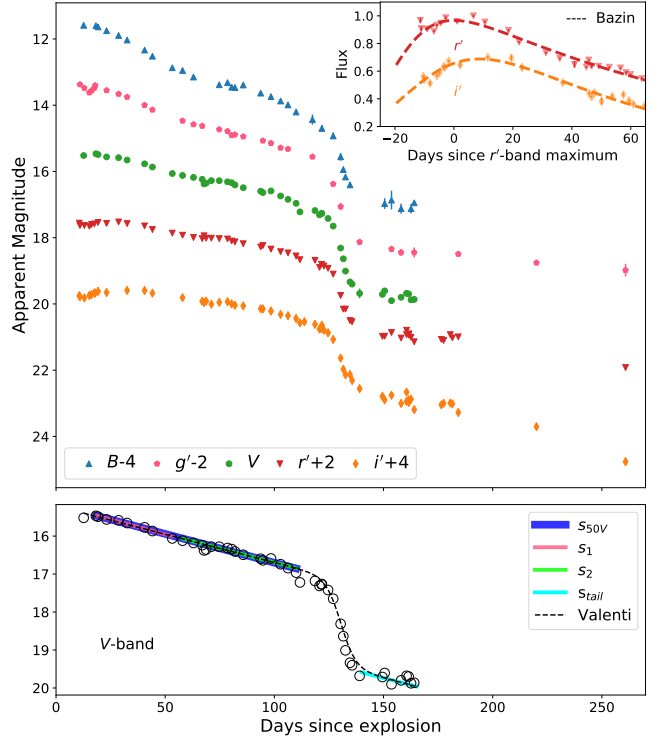


**Figure 2.** *Top Panel* :  $Bg'Vr'i'$  light curves of SN 2015an offset by a constant value in magnitude in different bands. In the inset plot, the fits to estimate the rise time in the  $r'i'$  bands are shown. *Bottom Panel* : The fits to the overall decline rate post-maximum up to the fall-off from plateau ( $s_{50V}$ ), early cooling phase ( $s_1$ ), the recombination phase ( $s_2$ ), the radioactive tail phase ( $s_{tail}$ ) and the best-fit to the  $V$ -band light curve using the function from Valenti et al. (2016) are shown.

**Table 6.** The best-fit slopes in the different phases of the  $V$ -band light curve of SN 2015an measured between start and end phase as well as the best-fit parameters using Valenti et al. (2016) expression are listed. All slopes are measured in magnitudes per 50d.

Slope	Decline rate	Start phase	End phase
$s_1$	$0.78 \pm 0.02$	15	55
$s_2$	$0.62 \pm 0.02$	55	120
$s_{50V}$	$0.74 \pm 0.01$	15	120
<hr/>			
$t_{PT}$ (d)	$a_0$ (mag)	$w_0$ (d)	$p_0$ (mag/d)
$130.4 \pm 0.3$	$2.30 \pm 0.05$	$3.4 \pm 0.4$	$0.0148 \pm 0.0004$

duration of the transition phase (typically  $6 \times w_0$ ), the time from explosion to the transition point from the plateau to the tail phase ( $t_{PT}$ ) and the slope of the radioactive tail phase ( $p_0$ ). The best fit parameters are summarized in Table 6 and the best fits are shown in the bottom panel of Fig. 2.

Anderson et al. (2014b) found the average decline rates for a SNe II sample to be  $s_1 = 1.32 \pm 0.75$  and  $s_2 = 0.64 \pm 0.47$  mag/50 d. The decline rates ( $s_1$  &  $s_2$ ) of SN 2015an suggests that this event is consistent with slowly declining SN II (Anderson et al. 2014b), while the Faran et al. (2014) criterion of classifying events with  $s_{50V} > 0.5$  as IIL, places SN 2015an ( $s_{50V} = 0.74$  mag/50 d) under the linearly declining SNe II. The magnitude drop ( $a_0$ ) of SN 2015an,  $2.30 \pm 0.05$  mag, lies

<sup>3</sup> <https://www.authorea.com/users/598/articles/6566>

**Table 7.** Parameters of the SNe II sample.

Supernova	Parent Galaxy	Distance <sup>†</sup> (Mpc)	$A_V^{tot}$ (mag)	Ref.
1987A	LMC	0.05	0.60	1
2005cs	M51	7.1 (1.2)	0.34	2,3
2009bw	UGC 2890	20.2 (0.6)	0.96	4
2009N	NGC 4487	19.8 (1.1)	0.403	5
LSQ13fn	LEDA 727284	264 (5.3)	0.167	6
2013by	ESO 138-G10	14.74 (1.0)	0.60	7
2013ej	NGC 628	9.6 (0.7)	0.19	8
2017eaw	NGC 6946	5.6 (0.1)	1.271	9

<sup>†</sup> In the  $H_0 = 73.48 \text{ km s}^{-1} \text{ Mpc}^{-1}$  scale.

References: (1) Hamuy & Suntzeff (1990), (2) Pastorello et al. (2006), (3) Pastorello et al. (2009), (4) Inserra et al. (2012), (5) Takáts et al. (2014), (6) Polshaw et al. (2016), (7) Valenti et al. (2015), (8) Huang et al. (2015); Bose et al. (2015); Yuan et al. (2016); Dhungana et al. (2016), (9) Szalai et al. (2019)

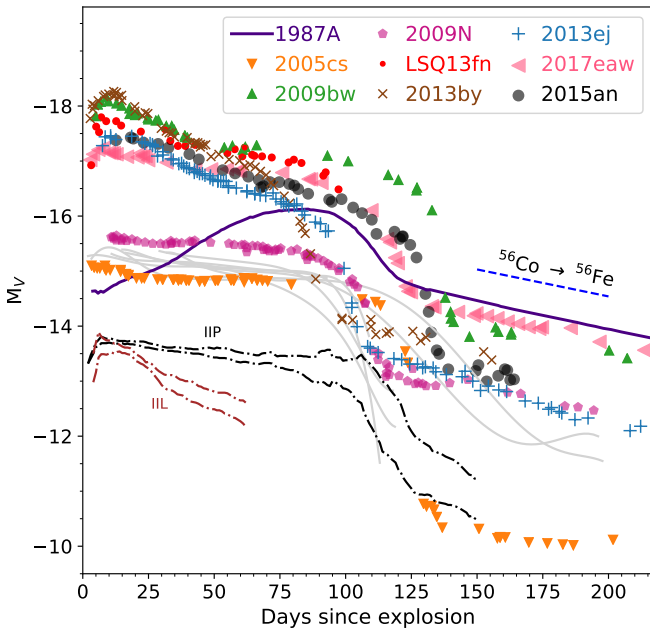


**Figure 3.** Comparison of absolute  $V$ -band light curves of SN 2015an with other Type II SNe. The magnitudes are corrected for distance and reddening as listed in Table 7. The radioactive decay line assuming full trapping of photons is shown with a dashed line. The dash-dotted lines depicts the range of slopes of Type IIP and IIL SNe as presented in Faran et al. (2014). The grey lines are the low-order Legendre fits to the light curve of low-luminosity SNe ( $M_V > -15.5 \text{ mag}$ ) from Anderson et al. (2014b)

in the range of 1-2.6 mag as suggested for SNe II in Valenti et al. (2016).

In order to discern the position of SN 2015an in the SNe II diversity, a sample of events is assembled, to be used as reference and listed in Table 7. The reference sample is composed of – SN 1987A: the II-pec SN, SN 2005cs representing the low-luminosity events, SN 2009N: a member of the intermediate luminosity events, SN 2009bw: a luminous and long plateau SN IIP, SN 2013by: a prototypical IIL, SN 2013ej: a fast declining IIP/L, LSQ13fn: a SN IIP exhibiting several peculiar characteristics and SN 2017eaw: a prototypical IIP. We have compared the absolute mag-

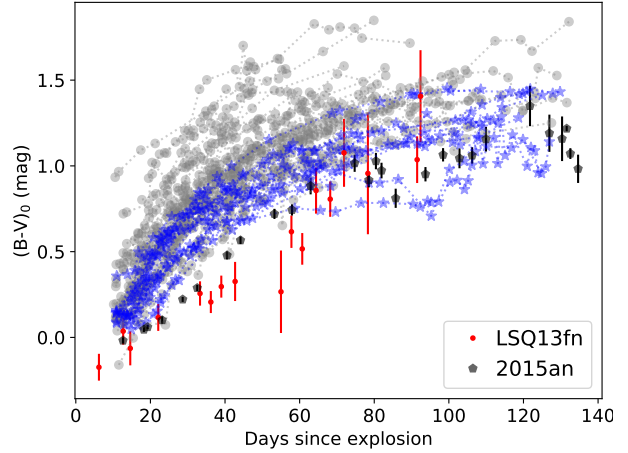


**Figure 4.** The  $(B-V)_0$  colour evolution of SN 2015an compared with a sample of SNe II from de Jaeger et al. (2018) (shown in grey) and a subset of this sample with negligible host extinction (shown with blue stars). The colour evolution of SN LSQ13fn is also shown, which falls at the bluer end. All the  $(B-V)$  colours are corrected only for Galactic reddening.

nitude of SN 2015an with that of the reference sample and low-luminosity SNe ( $M_V > -15.5 \text{ mag}$ ) from Anderson et al. (2014b) in Fig. 3, and we see that SN 2015an stands among the brighter SNe II, with an absolute magnitude at 50 d,  $M_V^{50} = -16.83 \pm 0.04 \text{ mag}$ , similar to SN 2017eaw. In Fig. 3, the range of slopes possible for the sub-types IIP and IIL from the study of Faran et al. (2014) is shown with dash-dotted lines and it is clear that the LC of SN 2015an conforms to the IIL class.

The  $(B-V)_0$  colour evolution of SN 2015an is shown in Fig. 4, along with the sample of 57 SNe II from de Jaeger et al. (2018). The blue stars are the members of the sub-sample composed of events which are located far away from the host galaxy nuclei and exhibit inconspicuous  $\text{Na I D}$  absorption. For a comparison, we also plot the colours of LSQ13fn, which are at the bluer end. Clearly, SN 2015an falls on the bluer edge of the sample, displaying an evolution typical of SNe II. The  $(B-V)_0$  colour becomes redder rapidly at early times when the temperature drops quickly following a power law in time, until the commencement of the recombination phase at around 55 d. Since the temperature variation is not much apparent in the plateau phase, colour changes slowly in this phase.

The  $^{56}\text{Ni}$  mass is estimated from the tail bolometric luminosity following Hamuy (2003) using the tail  $V$ -band magnitudes. The tail luminosity ( $L_t$ ) obtained from the  $V$ -band magnitudes using the bolometric correction factor given in Hamuy (2003) at 5 epochs – 158.2, 160.7, 161.7, 162.7 and 164.2 d are  $6.11 \pm 0.49 \times 10^{40}$ ,  $6.82 \pm 0.55 \times 10^{40}$ ,  $6.70 \pm 0.54 \times 10^{40}$ ,  $5.69 \pm 0.46 \times 10^{40}$  and  $5.75 \pm 0.46 \times 10^{40} \text{ erg s}^{-1}$  respectively, which corresponds to a mean  $^{56}\text{Ni}$  mass of  $0.021 \pm 0.010 M_\odot$ . The  $^{56}\text{Ni}$  mass of SNe 2013ej and 2017eaw with similar plateau magnitudes ( $M_V^{50} = -16.61$  and  $-16.85 \text{ mag}$ , respectively) as SN 2015an are  $0.018$  and  $0.045 M_\odot$ , respectively. Thus SN 2015an is more similar to the linearly declining SN 2013ej than the slowly declining SN 2017eaw. The  $^{56}\text{Ni}$  yield of SN 2009N ( $0.020 M_\odot$ ) is the same as SN 2015an, however, the former is an intermediate luminosity SN, with a much lower plateau magnitude ( $-15.59 \text{ mag}$ ).

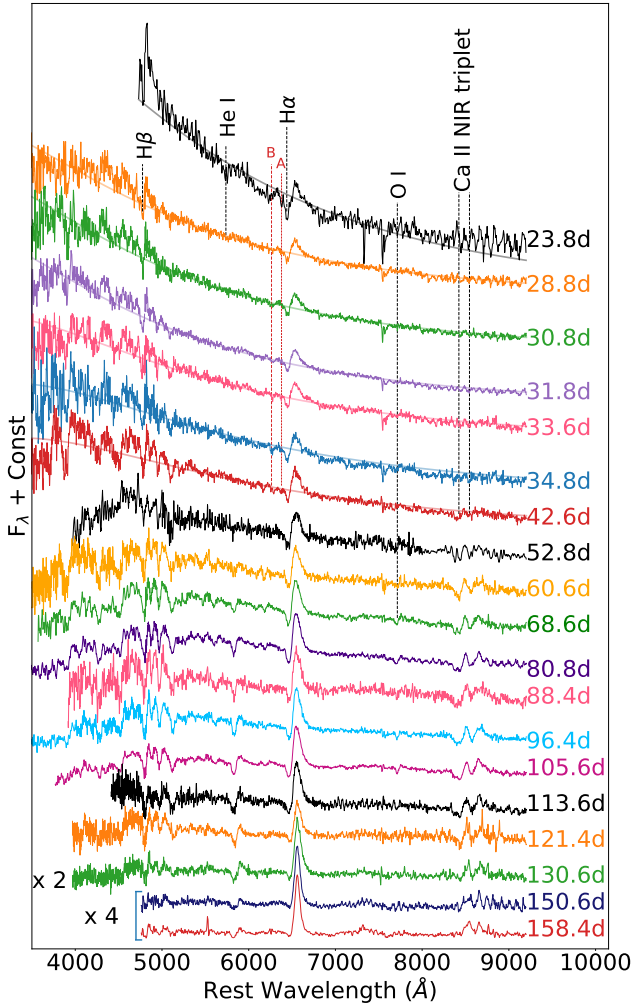


**Figure 5.** The spectral evolution of SN 2015an from 23.8 d to 158.4 d is shown. The spectra are corrected for redshift and Galactic extinction. The conspicuous blue continuum in the early spectra are fitted with a blackbody model to estimate the temperature during these phases. The absorption dips bluewards of the  $H\alpha$  profile are marked as ‘A’ and ‘B’.

#### 4 SPECTRAL ANALYSIS

Fig. 5 shows the spectral evolution of SN 2015an from 23.8 to 158.4 d after explosion. The blue continuum in SN 2015an persists longer, up to 42.6 d, than other normal SNe II. Line identifications were made following Leonard et al. (2002). The continuum is fitted with a blackbody function to determine the temperature (shown with solid lines for the first 7 epochs). The temperature is around 8800 K at 28.8 d and then gradually drops to 5600 K at 68.6 d and remains nearly constant afterwards. Prominent  $H\alpha$  and weak He I  $\lambda 5876$  feature can be discerned in the earliest spectrum. While  $H\alpha$  grows with time, the He I feature disappears after the 28.8 d spectrum. The Fe II  $\lambda\lambda 4094, 5018, 5169$  and Ca II H&K emerge in the 28.8 d spectrum, weak features of Sc II  $\lambda 6245$  and Ca II NIR triplet becomes detectable from the 42.6 d spectrum, the Na I D and Ba II  $\lambda 6142$  features becomes conspicuous from the 60.6 d spectrum and the O I  $\lambda 7774$  lines becomes visible from the 68.6 d spectrum. Fe II and Sc II remains visible up to 130.6 d, however the Ba II and O I lines

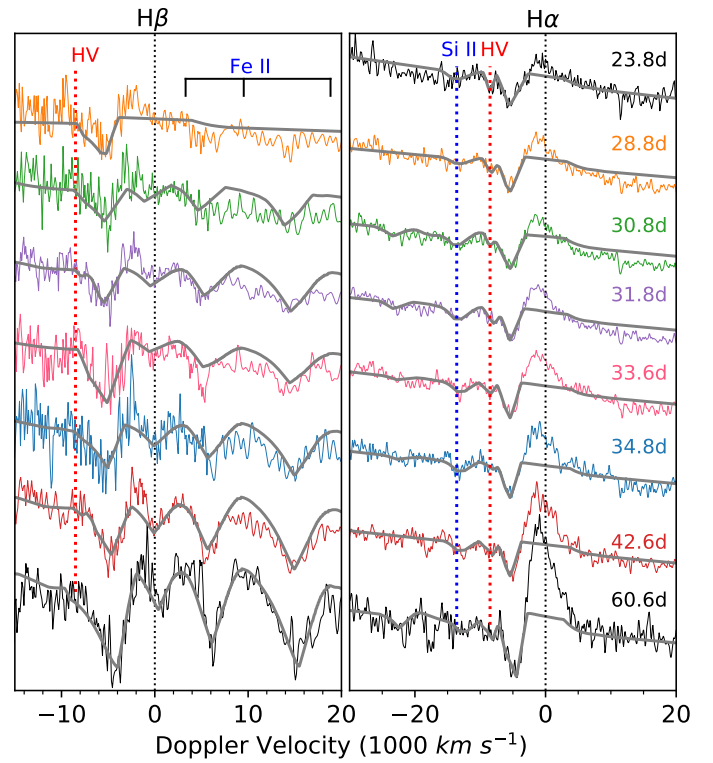


**Figure 6.** Evolution of  $H\alpha$ ,  $H\beta$  emission line profiles during the photospheric phase. The SYN++ model fits to the spectra are shown with grey solid lines. The Si II (‘B’) and high velocity (HV) features (‘A’) are conspicuous up to the 50 d spectrum and are shown with dashed lines.

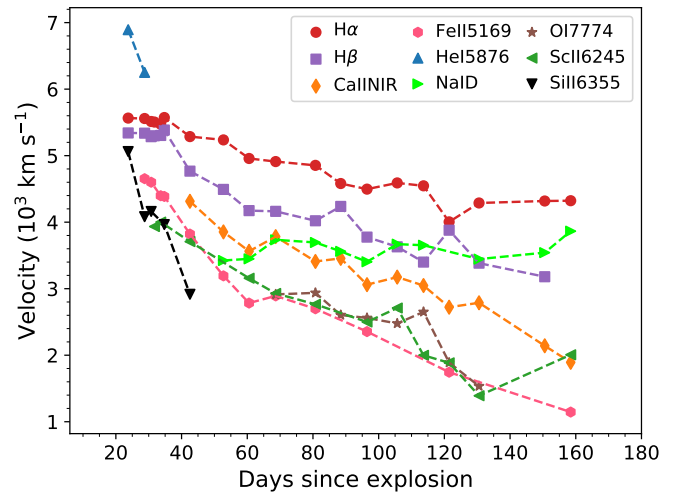


**Figure 7.** Line velocity evolution of  $H\alpha$ ,  $H\beta$ , He I, Fe II, Sc II, Ca II NIR, Na I D and Si II lines. The velocities are estimated from the absorption minima of these profiles.

becomes undetectable after the 105.6 d spectrum. Most of these metal lines disappears in the last two spectra (150.6 and 158.4 d), except Na I D and Ca II NIR triplet.

The evolution of  $H\alpha$  and  $H\beta$  lines from 23.8 to 60.6 d is shown in Fig. 6 in the velocity domain and centered at the rest wavelengths of these lines along with the SYN++

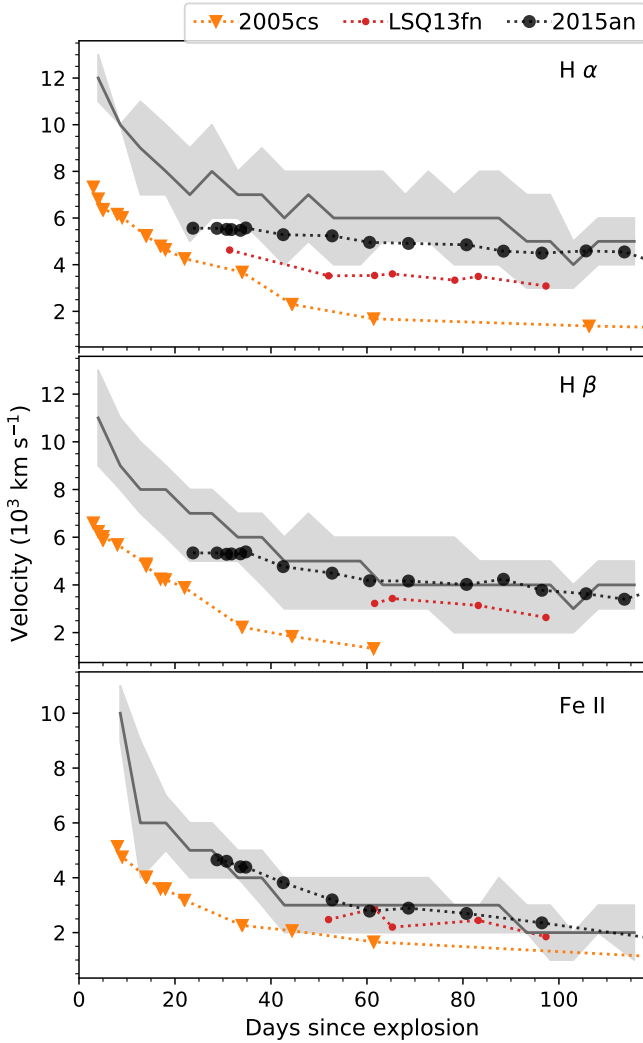


**Figure 8.** A comparison of the velocity of SN 2015an to SNe 2005cs, LSQ13fn and the mean velocity (grey) of 122 IIP/IIL SNe (Gutiérrez et al. 2017b) for  $H\alpha$  (top panel),  $H\beta$  (middle panel) and Fe II ( $\lambda 5169$ ; bottom panel). The light grey regions represent the standard deviations of the mean velocities of the sample.

(Thomas et al. 2011) fits. The emission peak of  $H\alpha$  is shifted by  $\sim 1100 \text{ km s}^{-1}$  in these phases. Two absorption dips on the blue side of the  $H\alpha$  absorption component is visible from the 23.8 d spectrum until 42.6 d and hardly detectable in the 60.6 d spectrum. Such features have been reported at both early and late photospheric epoch in a number of SNe II, and has been termed ‘cachito’ (Gutiérrez et al. 2017a). In case of a non-evolving feature, the dip is interpreted to be high velocity (HV) component of  $H\alpha$ , which usually appears in the late photospheric phases and an evolving component is thought to be originating from Si II  $\lambda 6355$ , which typically appears in the early phases. However, rarely these two features have been observed at coeval epochs. For SN 2015an, the feature ‘A’ does not evolve with time, while the feature ‘B’ shows an evolving velocity similar to the metal lines (see Fig. 7), and hence we identify the feature ‘A’ as the HV component of  $H\alpha$  and the feature ‘B’ as Si II  $\lambda 6355$ . This is

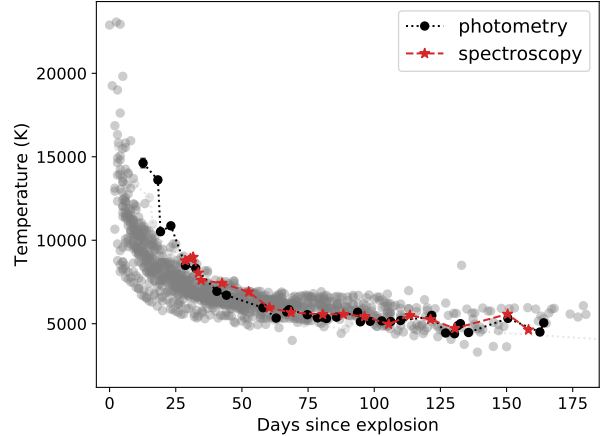


**Figure 9.** Comparison of the temperature evolution of SN 2015an estimated by fitting a blackbody to the photometric and spectroscopic fluxes with a collection of SNe II from Faran et al. (2018).

further confirmed by the SYN++ models fitted to the 23.8 to 60.6 d spectra, where we used a constant HV component ( $\sim 8500 \text{ km s}^{-1}$ ) in addition to the evolving normal velocity component, to reproduce the  $H\alpha$  absorption component. While the HV feature is apparent in  $H\alpha$ , it is inconspicuous in  $H\beta$ , which is possibly due to the low opacity of  $H\beta$  in the circumstellar wind (Chugai et al. 2007), producing rather a broadened absorption feature of  $H\beta$ .

The velocity evolution of the discernible ions as measured from the shift in the absorption minima from the rest wavelength of these lines are shown in Fig. 7, along with the feature identified as Si II  $\lambda 6355$ . The He I line detected in the two earliest spectra has the highest expansion velocity ( $\sim 6890$  and  $6250 \text{ km s}^{-1}$  at 23.8 and 28.8 d, respectively) among the ions. The  $H\alpha$  and  $H\beta$  velocities are nearly similar up to 40 d, and higher than the velocities of the metal lines, suggesting its formation in the outer higher velocity layer of the ejecta. The remarkable characteristic of SN 2015an is, however, the low expansion velocity of H I ( $5250 \pm 260 \text{ km s}^{-1}$  at 50 d) as compared to SNe II family (median  $H\alpha$  velocity at 50 d post-explosion:  $7300 \text{ km s}^{-1}$ , Gutiérrez et al. 2017a) with a nearly flat evolution.

## 4.1 Comparison with other SNe II

### 4.1.1 Velocity and temperature evolution

Fig. 8 shows the  $H\alpha$ ,  $H\beta$  and Fe II 5169 velocity evolution of SNe 2005cs, LSQ13fn and 2015an overplotted on the estimated mean velocities of the 122 IIP/L SNe from Gutiérrez et al. (2017b). The  $H\alpha$  velocity of SN 2015an lies in the lower edge of the velocity range of SNe II, with significantly low velocity ( $\sim 5500 \text{ km s}^{-1}$ ) at early phases as compared to the median velocity of the sample ( $\sim 7900 \text{ km s}^{-1}$ ). The  $H\alpha$  velocity of LSQ13fn falls outside the range of velocities of SNe II in the sample, but is still higher than the low-luminosity SN 2005cs by  $\sim 800 \text{ km s}^{-1}$  and  $\sim 1700 \text{ km s}^{-1}$  at early ( $< 30 \text{ d}$ ) and late phases ( $> 40 \text{ d}$ ), respectively. The H I line velocities of SN 2015an does not vary much and shows a nearly flat evolution. Nevertheless, the  $H\beta$  and Fe II velocity evolution of SN 2015an matches with the mean velocity



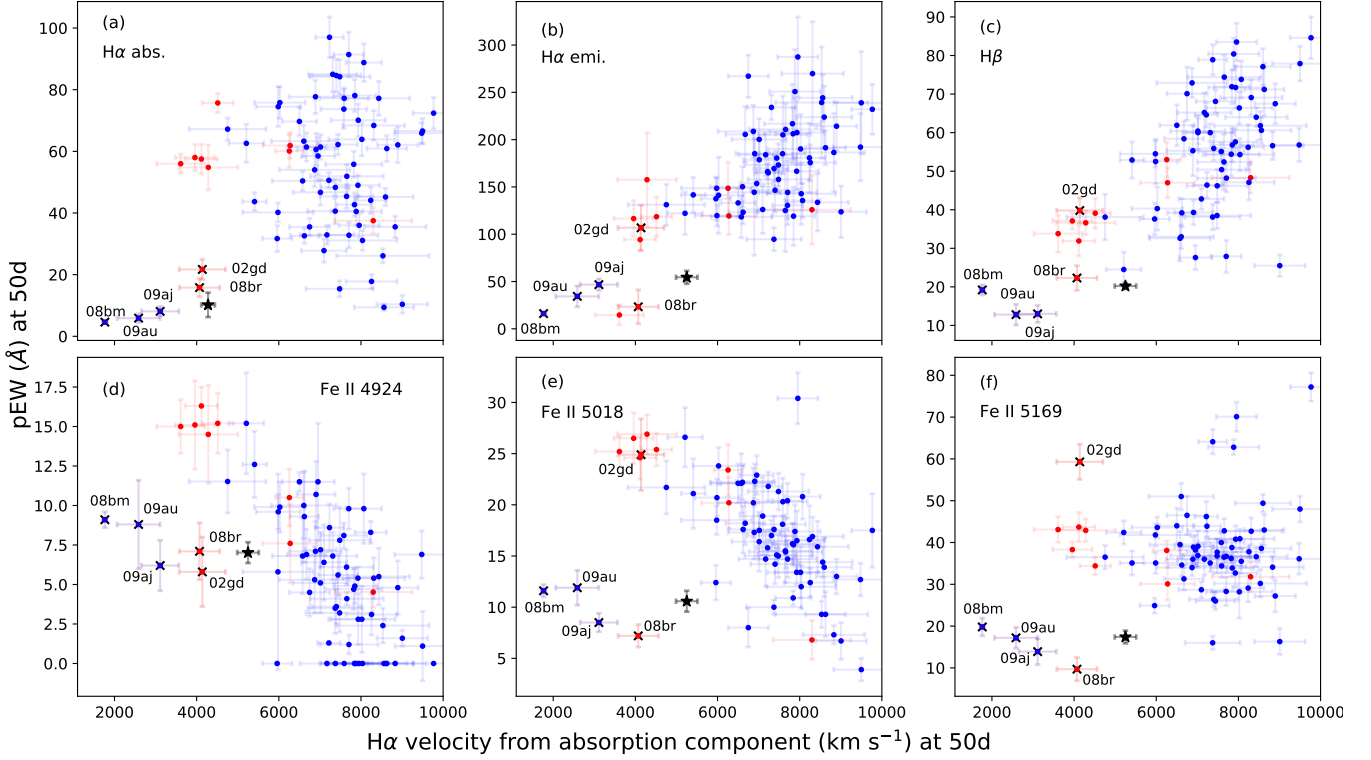


**Figure 10.** The pEW of the prominent features in the 50 d spectra of SN 2015an are plotted against the  $H\alpha$  velocity estimated from the shift in the absorption minima at 50 d (marked with  $\star$ ) and compared with the sample of [Gutiérrez et al. \(2017b\)](#). The low-luminosity SNe ( $-14 > M_V^{max} > -15.5$ ) are shown in red. SNe 2002gd, 2008bm, 2008br, 2009aj and 2009au, with small pEW of  $H\alpha$  and low  $H\alpha$  expansion velocity, similar to SN 2015an are marked with ‘x’.

evolution of the sample, except in the early phase ( $< 30$  d), where the velocity of  $H\beta$  falls on the lower limit of the mean velocity.

The temperature evolution of SN 2015an, obtained by performing blackbody fit to the SED constructed from photometric and spectroscopic fluxes, is shown in Fig. 9. The grey points depicts the evolution of temperature of a collection of 29 SNe II from [Faran et al. \(2018\)](#). Initially the temperature of SN 2015an (14600 K at 12.8 d) is higher than other SNe II at similar phases. The temperature of the sample at  $\sim 13$  d varies in the range of 6580 to 10840 K with a median temperature of  $\sim 9000$  K. Later than 40 d, when the SN enters the recombination phase, the temperature of SN 2015an is  $\sim 7400$  K still around 1000 K higher than the median temperature ( $\sim 6500$  K) of the sample. The blue (B-V) colour and the excess blue flux in the early spectra corroborates with the high temperature of SN 2015an in the early phase.

#### 4.1.2 Comparison of plateau spectra

SN 2015an displays some peculiar characteristics, in addition to the usual properties of SNe II, thereby necessitating the cognizance of the status of SN 2015an in the SNe II population before heading for the comparison with a sample of events. To this aim, we plotted the pseudo-equivalent widths (pEW) of the prominent lines vs  $H\alpha$  velocity at 50 d of SN 2015an along with a sample of 122 SNe II from [Gutiérrez](#)

[et al. \(2017b\)](#) in Fig. 10. This SN II sample exhibits a range of  $H\alpha$  expansion velocities ( $1500 < v_{H\alpha} < 9600$  km  $s^{-1}$ ) and pEWs of lines, presumably linked to the diversity in the explosion energies, progenitor radius and metallicity of SNe II. As noted in [Gutiérrez et al. \(2017b\)](#), the  $H\alpha$  velocity exhibits the strongest positive correlation with the pEW of the emission component of  $H\alpha$  and the absorption component of  $H\beta$  and negative correlation with pEW of Fe II  $\lambda 4924$  and Fe II  $\lambda 5018$ . In panel (a), SN 2015an lies at the lower left corner (small pEW and low  $v_{H\alpha}$ ), along with SNe 2002gd, 2008br, 2008bm, 2009aj and 2009au, clearly far off from the majority of SNe II. However, in panels (b) and (c), SN 2015an seems to fall in the trend of a positive correlation of expansion velocity with pEW of  $H\alpha$  emission component and  $H\beta$  absorption component, respectively. In the case of Fe II  $\lambda\lambda 4924, 5018, 5169$  (panels (d), (e) and (f)), SN 2015an lies intermediate to that of majority of SNe II and the four SNe on the left. Out of the five SNe from the lower left corner in panel (a), SNe 2008bm, 2009au and 2009aj shows unusually low velocities for their brightness and narrow emission lines at early phases, indicative of CSI at play. So, for comparison, we use the  $\sim 45$  d dereddened and de-redshifted spectra of SNe 2008bm, 2009aj and 2009au along with that of the low-luminosity SN 2005cs, the Type IIP SN LSQ13fn and the Type IIL SN 2014G. The spectra of SN 2015an obtained on 42.6 d and the comparison sample are shown in Fig. 11. While SN 2005cs shows well-developed metal lines, all other SNe exhibit comparatively

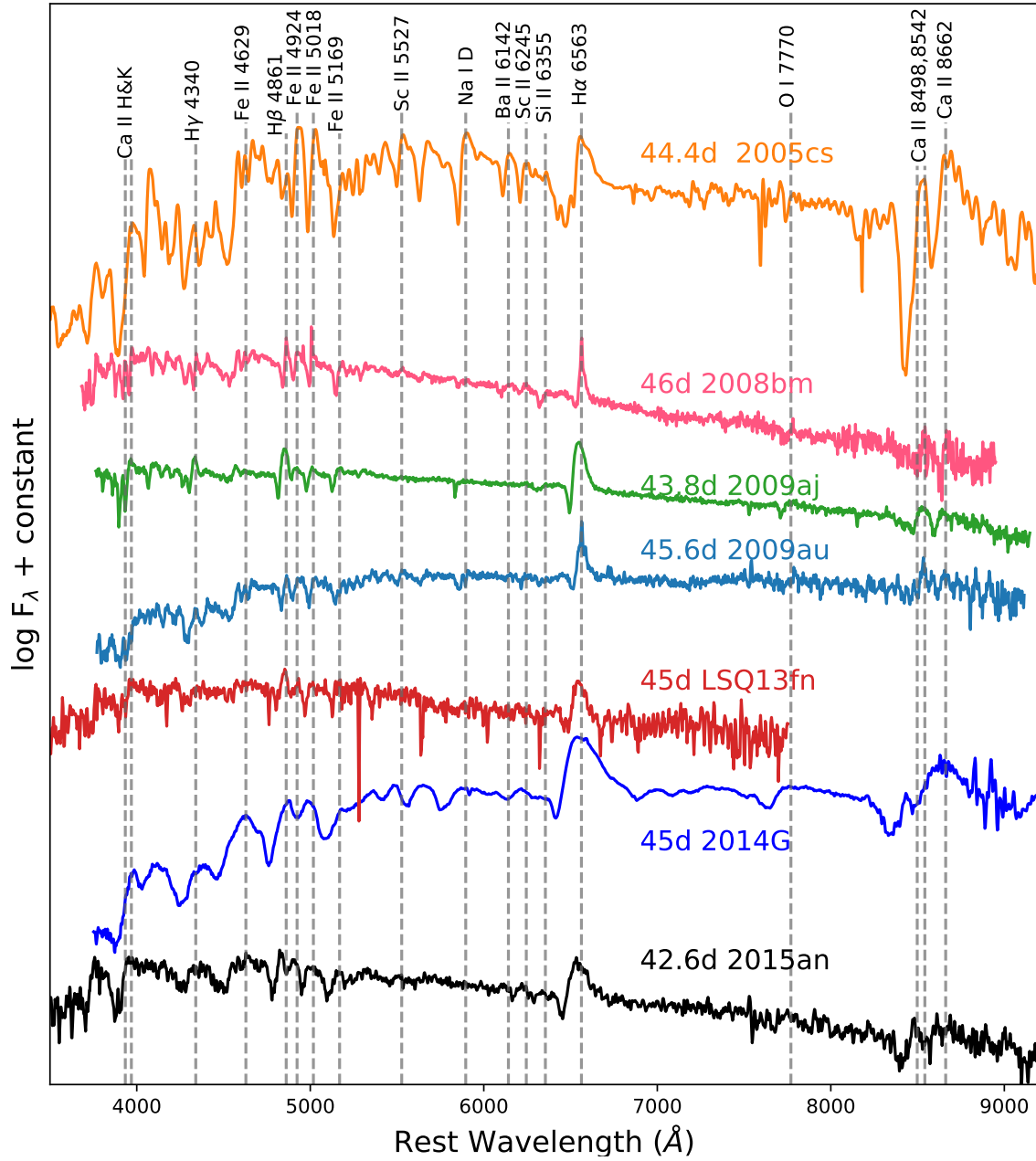


**Figure 11.** Comparison of mid-plateau spectrum (42.6 d) of SN 2015an with other SNe from the reference sample.

weaker metal lines. The continuum of SN 2015an matches well with that of SN LSQ13fn and neither of them has a conspicuous Na I D line at this phase, as compared to the other SNe. The SNe displaying weaker metal lines has enhanced continuum flux bluewards of 5200 Å, compared to SNe 2005cs and 2014G except SN 2009au.

Dessart et al. (2014) suggested that the SN progenitor metallicity plays a crucial role in the evolution of metal lines in the photospheric phase in that the SNe with low progenitor metallicity exhibit weaker metal features. Dessart et al. (2013) simulated model spectra by evolving a 15  $M_{\odot}$  ZAMS star up to the pre-SN stage at different metallicities (0.1, 0.4, 1.0, 2.0  $Z_{\odot}$ ). Comparing the 42.6 d spectrum of SN 2015an with these models we found the best match with 0.4  $Z_{\odot}$

model spectrum (pEW of Fe II  $\lambda$ 5018 in the 42.6 d spectrum of SN 2015an is 11.0 Å and that of the model spectrum at 41.1 d is 10.6 Å), which is overplotted on the spectrum of SN 2015an in the top panel of Fig. 12. Moreover, using a sample of 119 host H II regions Anderson et al. (2016) estimated the oxygen abundances and found a positive correlation between the host H II region oxygen abundance and pEW of Fe II  $\lambda$ 5018. In the bottom panel of Fig. 12, the time evolution of the mean pEW of Fe II  $\lambda$ 5018 of the sample of SNe II from Anderson et al. (2016) is shown along with its standard deviation (the black line and the shaded region), over which the thick solid lines are the time evolution of the pEW of Fe II  $\lambda$ 5018 in the different metallicity models of Dessart et al. (2013). The pEW measurements of

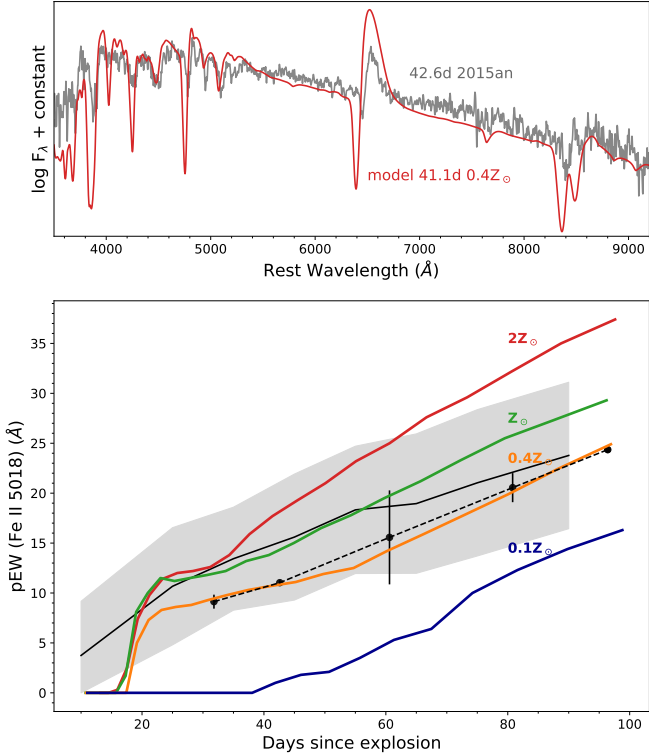


**Figure 12.** *Top Panel:* Comparison of a mid-plateau spectrum (42.6 d) of SN 2015an with the  $0.4 Z_{\odot}$  model spectrum of Dessart et al. (2013). *Bottom Panel:* The evolution of the pEW of Fe II  $\lambda 5018$  of SN 2015an is shown with dashed lines. The black line is the mean pEW of a sample of 119 SNe II from Anderson et al. (2016) and the shaded region shows the standard deviation about the mean. The time evolution of the pEWs of Fe II  $\lambda 5018$  of the four distinct metallicity models of Dessart et al. (2013) is shown with thick lines.

Fe II  $\lambda 5018$  in the spectra of SN 2015an is shown with a dashed line which traces the evolution of the  $0.4 Z_{\odot}$  model and is lower than the mean pEW of the sample.

## 5 DISTANCE

We implement the EPM to estimate the distance from early photometric and spectroscopic observations as outlined in Dastidar et al. (2018). The EPM rests on the assumption that the ejecta is homologously expanding and radiating as a diluted blackbody. Thus, the colour temperature ( $T_c$ ) and the angular radius ( $\theta$ ) were obtained by fitting diluted blackbody function to the spectral energy distribution constructed from the observed magnitudes, where the dilution factors were adopted from Dessart & Hillier (2005). Moreover, the filter response function needs to be convolved with the model blackbody function, to eliminate its effect from the observed broadband magnitudes. The convolved function can be expressed as a function of  $T_c$  and the coefficients were adopted from Hamuy et al. (2001). The photospheric velocities ( $v_{ph}$ ) were estimated from the minima of the absorption profile of H $\alpha$  in the first epoch (13.6 d from discovery) and Fe II  $\lambda 5169$  in the rest of the epochs (up to  $\sim 50$  d from discovery).

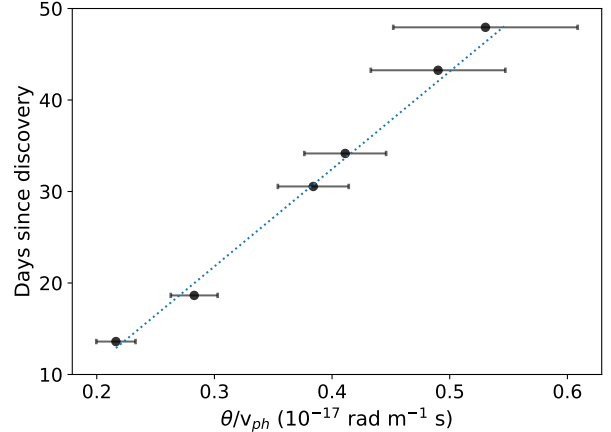


**Figure 13.** Distance determination with the EPM for SN 2015an, using Dessart & Hillier (2005) prescription for the dilution factors and the  $BV$  observations. The distance and the explosion epoch are obtained from the best fit.

The distance and the time of explosion  $t_0$  can then be estimated from the slope and y-intercept, respectively, of the following expression:

$$t = D(\theta/v_{ph}) + t_0 \quad (1)$$

The linear fit to the data is shown in Fig. 13 and the distance and explosion epoch estimates from the fit are  $29.8 \pm 1.5$  Mpc and  $2457268.5 \pm 1.6$  d (2015 September 03 UT), respectively.

## 6 SEMI-ANALYTICAL MODELLING OF THE BOLOMETRIC LIGHT CURVE

To generate the observed bolometric light curve, first the observed fluxes were corrected for distance and reddening using the values given in Table 1. Then SED at different epochs was constructed encompassing the fluxes from the UV to the IR wavelengths. Due to the unavailability of UV and IR data, we extrapolated the SED constructed in the optical bands, approximating it as a blackbody, to the UV and IR bands, following the same prescription as used in the direct integration method in Lusk & Baron (2017). At late phases, a linear extrapolation is performed in the UV regime. The decline rate of the radioactive tail in the bolometric light curve is found to be 0.0140 mag/d which is steeper than 0.0098 mag/d, indicating incomplete trapping of the  $\gamma$ -rays produced by the radioactive decay of  $^{56}\text{Co} \rightarrow ^{56}\text{Fe}$ .

We used semi-analytical modelling of Nagy et al. (2014); Nagy & Vinkó (2016) to model the bolometric light curve of SN 2015an. To synthesize the fast initial decline and the late phase of SNe II, this model invokes a two component structure of ejecta, where a massive core is surrounded by a low mass envelope.

We used a constant density profile for the core and a power law density profile for the envelope. The opacity values for the core and the shell are kept fixed to the average opacity recommended for SNe IIP ( $\kappa_{core}=0.2 \text{ cm}^2 \text{ g}^{-1}$  and  $\kappa_{shell}=0.38 \text{ cm}^2 \text{ g}^{-1}$ , Nagy 2018). The estimated best fit parameters are the initial radius ( $2.7 \times 10^{13} \text{ cm} \sim 388 R_{\odot}$ ), ejecta mass  $M_{ej}$  ( $12 M_{\odot}$ ) and total energy (1.8 foe). Assuming the remnant mass to be  $1.5\text{-}2.0 M_{\odot}$ , the minimum

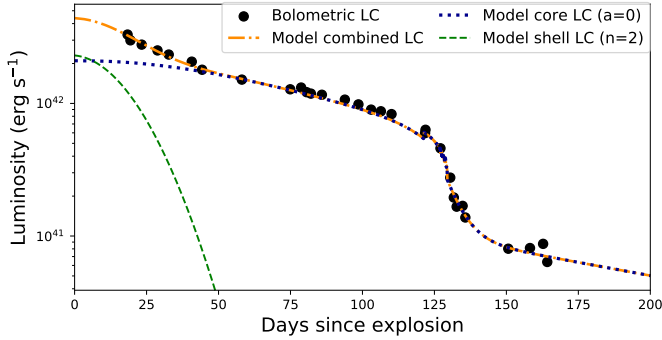


**Figure 14.** The observed bolometric LC of SN 2015an and the best fit two component analytical model of Nagy & Vinkó (2016).

**Table 8.** The best fit core and shell parameters for true bolometric light curve of SN 2015an using Nagy & Vinkó (2016).

Parameter	Core	Shell	Remarks
$R_0$ (cm)	$2.7 \times 10^{13}$	$9.0 \times 10^{13}$	Initial radius of ejecta
$T_{rec}(K)$	7000	-	Recombination temperature
$M_{ej}$ ( $M_{\odot}$ )	12	0.3	Ejecta mass
$E_{th}(foe)$	0.9	0.04	Initial thermal energy
$E_{kin}(foe)$	0.9	0.06	Initial kinetic energy
$M_{Ni}$ ( $M_{\odot}$ )	0.02	-	Initial $^{56}\text{Ni}$ mass
$\kappa$ ( $\text{cm}^2 \text{g}^{-1}$ )	0.2	0.38	Opacity
$A_g$ ( $\text{day}^2$ )	$3.0 \times 10^5$	$1 \times 10^{10}$	Gamma-ray leakage

ZAMS mass of the progenitor is  $14 M_{\odot}$ . The best-fit model is over-plotted on the bolometric LC in Fig. 14 and the parameters for the core and the shell are listed in Table 8. In the top panel of Fig. 15, the total energy of SN 2015an ( $E_{tot} = E_{kin} + E_{th}$ ) is plotted against the ejecta mass, along with that derived for other SNe using hydrodynamic modelling (Utrobin & Chugai 2013; Pumo et al. 2017) and SNEC models (Morozova et al. 2018). SN 2015an falls in the trend of the positive correlation between the two parameters. In the bottom panel of Fig. 15, the  $^{56}\text{Ni}$  mass is plotted against  $E_{tot}$ , where we find that compared to its energy, the  $^{56}\text{Ni}$  mass yield should have been higher.

## 7 DISCUSSION

As discussed above, SN 2015an exhibits some peculiar features in addition to the regular properties of SNe II. The  $\text{H}\alpha$  expansion velocity of SN 2015an in the early phases is comparatively lower than other SNe II of similar luminosity. High velocity component of  $\text{H}\alpha$  is conspicuous at the early phases, which is not commonly observed in early SN II spectrum. Moreover, the persistence of the excess in flux bluewards of  $5200 \text{ \AA}$  up to  $\sim 43 \text{ d}$ , is also atypical of SNe II. We discuss below these properties of SN 2015an and its possible implications.

### 7.1 Collocation of SN 2015an in the SN II parameter space

In Fig. 16, we use samples of SNe II from recent studies to discern the position of SN 2015an in the SN II diver-

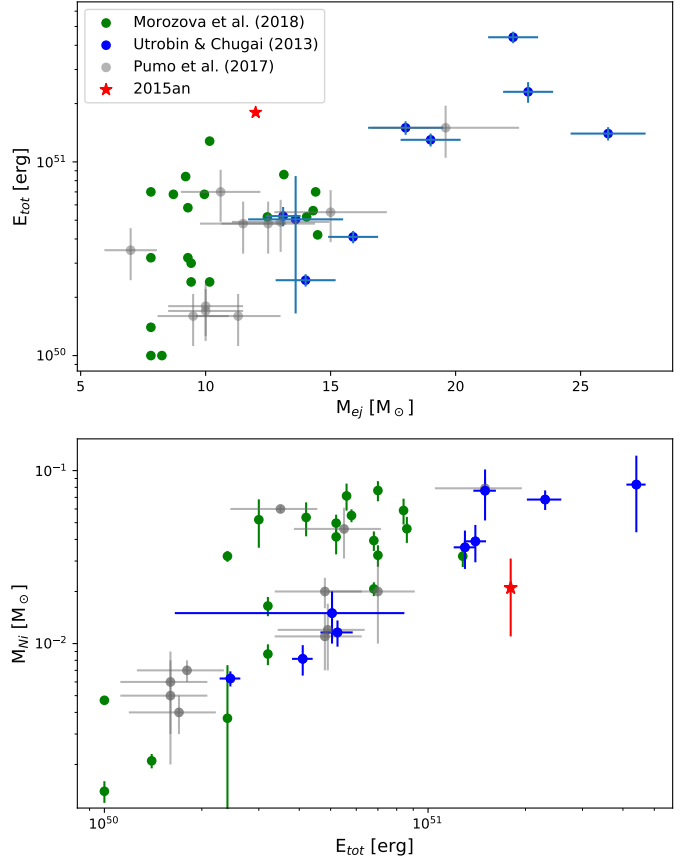


**Figure 15.** The total explosion energies of SNe ( $E_{tot} = E_{kin} + E_{th}$ ) are plotted against the ejecta masses and the ejected  $^{56}\text{Ni}$  masses of a sample of SNe from Utrobin & Chugai (2013); Pumo et al. (2017); Morozova et al. (2018)

sity. The regression line for the literature sample, excluding SNe LSQ13fn and 2015an, is shown in grey, the shaded region gives the  $3\sigma$  confidence interval for the regression coefficients and the dotted and dashed lines are the  $1\sigma$  and  $3\sigma$  prediction interval, respectively, for the regression model. The Pearson correlation parameters listed in the figure are also estimated using the literature samples.

In panel (a) of Fig. 16, the expansion velocity of Fe II  $\lambda 5169$  and absolute magnitude in the  $I$ -band of SN 2015an (obtained by converting the  $i$ -band magnitude to  $I$ -band magnitude using the transformation equation in Jordi et al. (2006)) at 50 d are shown, along with that of SN LSQ13fn and using the sample of Nugent et al. (2006) and Polshaw et al. (2015). SN LSQ13fn lies outside the  $3\sigma$  prediction band, which implies that this event has a much lower expansion velocity as compared to its luminosity. SN 2015an, on the other hand, is fainter than SN LSQ13fn by  $\sim 0.4 \text{ mag}$  and with an expansion velocity higher by  $600 \text{ km s}^{-1}$  than SN LSQ13fn, manages to settle itself right over the  $3\sigma$  prediction limit.

In Fig. (b), the absolute magnitude in  $V$ -band at 50 d is plotted against the logarithm of  $^{56}\text{Ni}$  mass for a sample of SNe from the literature (Hamuy 2003; Spiro et al. 2014; Valenti et al. 2016; Singh et al. 2018). Both SNe LSQ13fn and 2015an lies just outside the  $1\sigma$  prediction limit but well within the  $3\sigma$  prediction interval.

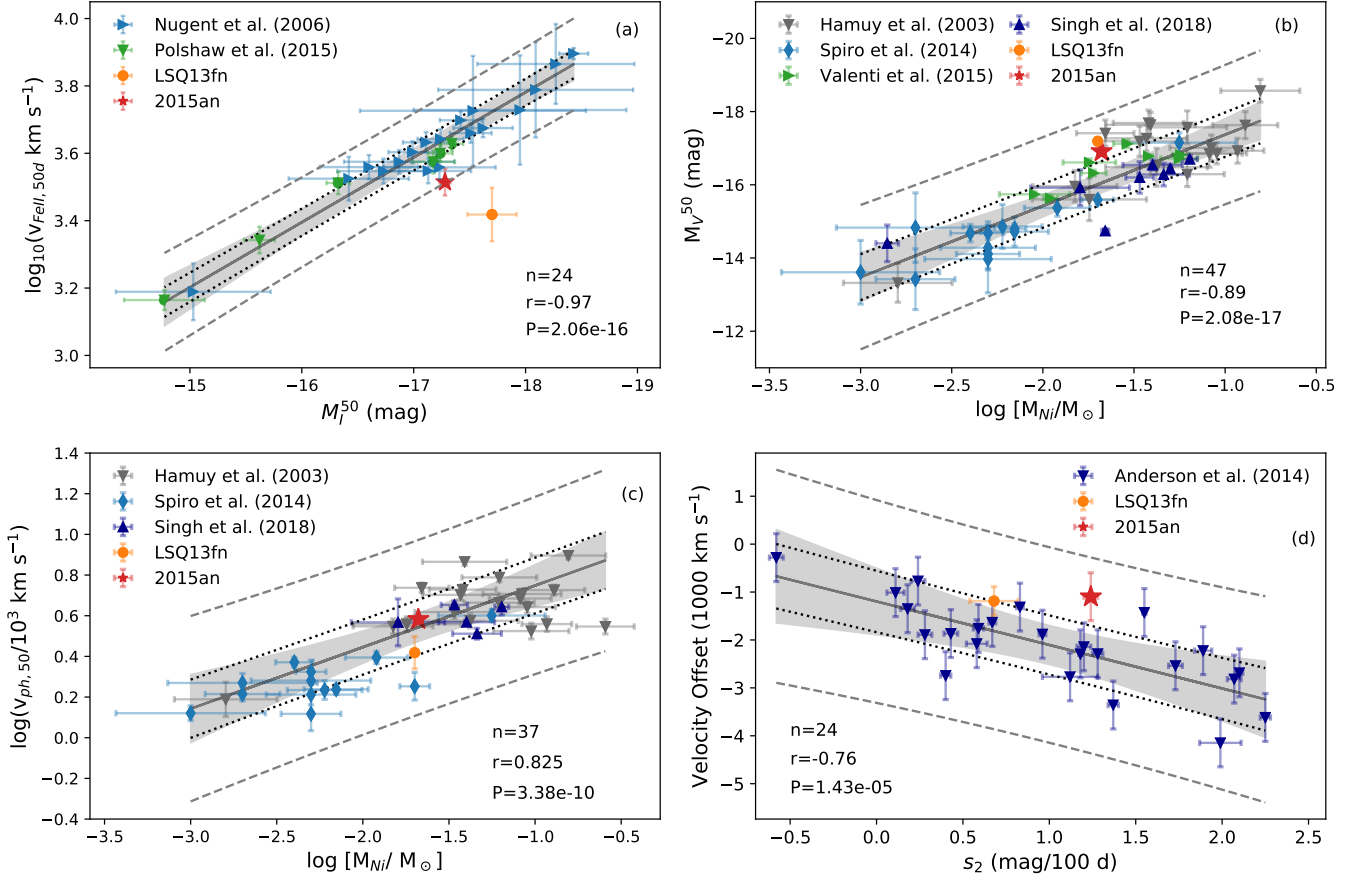


**Figure 16.** The collocation of SN 2015an in the correlation plots among absolute magnitude at 50 d ( $M_I^{50}$ ), the photospheric velocity at 50 d ( $v_{ph,50}$ ),  $^{56}\text{Ni}$  mass,  $\text{H}\alpha$  velocity offset from emission peak at 30 d and the decline rate of the V-band light curve in plateau phase ( $s_2$ ) in mag/100d is shown along with the sample of SNe II from Hamuy (2003); Nugent et al. (2006); Spiro et al. (2014); Anderson et al. (2014a); Polshaw et al. (2015); Valenti et al. (2016); Singh et al. (2018). The shaded region shows the  $3\sigma$  confidence interval, while the dotted and dashed line shows the 1 and  $3\sigma$  prediction limits, respectively. For each panel, n is the number of events, r is the Pearson correlation coefficient, and P is the probability of detecting a correlation by chance.

In Fig. (c), the photospheric velocity is plotted against the logarithm of  $^{56}\text{Ni}$  mass for a sample of SNe (Hamuy 2003; Spiro et al. 2014; Singh et al. 2018). In this case, we find both SNe LSQ13fn and 2015an lie within the  $1\sigma$  prediction interval.

In Fig. (d), the emission peak velocity offset of  $\text{H}\alpha$  at 30 d is plotted against the decline rate in the plateau phase ( $s_2$ ) using the sample from Anderson et al. (2014a), where the faster declining SNe have higher offsets. This is expected as faster declining SNe have a steeper ejecta density structure, enhancing the occultation of the receding part of the ejecta, thereby shifting the emission peak to the bluer wavelengths. With a decline rate ( $s_2$ ) of  $1.24 \pm 0.04$  mag/100 d, the emission peak of  $\text{H}\alpha$  in SN 2015an has a velocity offset smaller by about  $1000 \text{ km s}^{-1}$  than the mean offset of the sample, possibly due to its low expansion velocity.

Thus, the normal luminosity of SN 2015an in conjunction with its lower expansion velocity and lower  $^{56}\text{Ni}$  mass yield, suggests the existence of an external source boosting the luminosity of this event, most likely the interaction between the ejecta and CSM.

## 7.2 Early Circumstellar Interaction

For SN 2015an, we do not have any spectrum in the first three weeks after explosion. The first spectrum obtained on  $\sim 23.8$  d is dominated by blue continuum. Moreover, a notch bluewards of the  $\text{H}\alpha$  absorption feature is clearly discernible up to 42.6 d spectrum (Fig. 6). This feature is identified as the high velocity feature (HV) of  $\text{H}\alpha$  at  $8500 \text{ km s}^{-1}$  considering its non-evolving nature and further substantiated in the SYN++ modelling. The HV feature is attributed to the excitation of the outer recombined part of the ejecta with X-rays from the reverse shock as a result of the interaction of ejecta and circumstellar material (Chugai et al. 2007). SN 2015an also shows bluer colour and higher temperature, in comparison to a sample of SNe II at coeval epochs (Figs. 4, 9), which also indicates an interaction of SN ejecta with a nearby CSM, converting the ejecta kinetic energy to thermal energy.

The HV feature, however, is not apparent in the early phase of most SNe II. The appearance of this feature in SN 2015an at early times may be attributed to the low expansion velocity of hydrogen. A low velocity ejecta will take longer time to cover the nearby CSM. Once the CSM is tra-

versed by the ejecta, the HV feature is expected to diminish. It may again reappear as the ejecta becomes transparent, depending on the density of the CSM.

### 7.3 Low metallicity progenitor

The other remarkable feature of SN 2015an is the presence of weak metal lines in the photospheric phase, particularly Fe II  $\lambda\lambda 5018, 5169$ . Dessart et al. (2013) showed that metallicity plays a crucial role in metal line formation in SN spectra, during the recombination phase, when the photosphere essentially samples the outer H envelope, that is relatively less affected by mixing or nuclear burning. While the pEW of the H I line will be dependent on both the CSI and metallicity, as CSI will broaden the absorption component and shallow H I lines are expected to form from a higher metallicity ejecta, the metal lines will be solely affected by the metallicity of the progenitor. Moreover, the excess of flux bluewards of 5200 Å in SN 2015an, in comparison to other SNe II (such as SNe 2005cs and 2014G) at coeval epochs, indicates a less efficient line blanketing in SN 2015an. These properties suggest a low-metallicity progenitor for SN 2015an. The progenitor metallicity can potentially affect the colour of SNe II as well. The sample study of host H II region of SNe II to obtain metallicity estimates by Anderson et al. (2016), suggests a strong correlation of the pEW of Fe II  $\lambda 5018$  with metallicity. We found SN 2015an to match best with the 0.4  $Z_{\odot}$  metallicity model of Dessart et al. (2013). This indicates that SN 2015an possibly originated from a sub-solar metallicity progenitor. Furthermore, since metallicity gradients in galaxies are found to be radially decreasing outwards (Henry & Worthey 1999), the location of SN 2015an at a deprojected radial distance of 13.9 kpc, suggests a lower metallicity environment for the progenitor of SN 2015an.

Finally, it is worth noting that some atypical features of SN 2015an, such as its higher photospheric temperature and persistence of blue spectrum later than usual, is related to the explosion time. Since we do not have early spectra of SN 2015an (obtained within two weeks of discovery), we could not impose strong pre-explosion constraints. If SN 2015an was discovered soon after explosion (than our adopted explosion epoch corresponding to 10 d before discovery), then the temperature and colour of SN 2015an would become more similar to normal SNe II. Nevertheless, a spectrum of SN II with a dominant blue continuum two weeks past discovery and normal luminosity in concurrence with low expansion velocity of H $\alpha$ , as in case of SN 2015an, is unusual.

## 8 SUMMARY

In this paper, we present the photometric and spectroscopic analysis of SN 2015an in the galaxy IC 2367. The striking feature of SN 2015an is its low H $\alpha$  expansion velocity in the early phases as compared to its brightness. The absolute magnitude of SN 2015an at 50 d is  $M_V^{50} = -16.83 \pm 0.04$  mag, which places this event among the brighter SNe II. The slope of the V-band light curve in the first 50 d is  $0.78 \pm 0.02$  mag, which is steeper than the slowly declining SNe II. The colour evolution of SN 2015an follows the same trend as SNe II family, however, this event is bluer in comparison to the rest

of the sample. The Ni mass derived from the tail luminosity is  $0.021 \pm 0.010 M_{\odot}$ .

The spectra of SN 2015an is apparently similar to the SNe II population with prominent H I P Cygni profiles, however the metal lines are comparatively weaker and the blue continuum lasts longer than typical SNe II. High velocity features have also been identified in the early spectra of SN 2015an, suggesting a possible role of CSI. The temperature derived from the photometric and spectroscopic SEDs is relatively higher than SNe II in the early phases, implying the conversion of the kinetic energy of ejecta to thermal energy in the ejecta-CSM interaction. The weak metal lines and the blue continuum is possibly associated with the metallicity of the progenitor, as sub-solar metallicity progenitor produces weaker metal lines (Dessart et al. 2013).

We used the expanding photosphere method and derived a distance of  $29.8 \pm 1.5$  Mpc to SN 2015an, which is in accord with the Virgo infall distance. The explosion parameters derived from the best fit semi-analytic model generated using the prescription of Nagy & Vinkó (2016) to the bolometric light curve yielded a total ejecta mass of  $\sim 12 M_{\odot}$ , a total explosion energy of 1.8 foe and an initial radius of  $388 R_{\odot}$ . The estimated initial radius is small as compared to other RSGs, and hence SN 2015an was expected to show faster cooling with a rapid transition from the early cooling phase to the plateau phase and a redder continuum. We infer that the combined effect of ejecta-circumstellar interaction and a low-metallicity progenitor is giving rise to the peculiar properties of SN 2015an. Furthermore, it becomes apparent that CSI is not only important for Type II<sub>n</sub> or some III<sub>L</sub>, but also low-velocity SNe II may have some interaction.

## ACKNOWLEDGMENTS

We thank Thomas de Jaeger, J. P. Anderson, C. P. Gutiérrez and V. P. Utrobin for sharing data. This research has made use of the NASA/IPAC Extragalactic Database (NED) which is operated by the Jet Propulsion Laboratory, California Institute of Technology, under contract with the National Aeronautics and Space Administration. We acknowledge the usage of the HyperLeda data base (<http://leda.univ-lyon1.fr>). DAH, CM, and GH were supported by NSF-1313484. This work makes use of data obtained by the LCO network. Research by SV is supported by NSF grants AST-1813176. SBP and KM acknowledges BRICS grant DST/IMRCD/BRICS/Pilotcall/ProFCheap/2017(G) for the present work. SBP and KM also acknowledge the DST/JSPS grant, DST/INT/JSPS/P/281/2018. KM acknowledges the support from Department of Science and Technology (DST), Govt. of India and Indo-US Science and Technology Forum (IUSSTF) for the WISTEMM fellowship and Dept. of Physics, UC Davis where a part of this work was carried out.

## REFERENCES

- Anderson J. P., et al., 2014a, *MNRAS*, **441**, 671
- Anderson J. P., et al., 2014b, *ApJ*, **786**, 67
- Anderson J. P., et al., 2016, *A&A*, **589**, A110
- Andrews J. E., Smith N., 2018, *MNRAS*, **477**, 74
- Barbon R., Ciatti F., Rosino L., 1979, *A&A*, **72**, 287

- Bazin G., et al., 2009, *A&A*, 499, 653
- Bose S., et al., 2015, *ApJ*, 806, 160
- Chevalier R. A., 1976, *ApJ*, 207, 872
- Chugai N. N., Chevalier R. A., Utrobin V. P., 2007, *ApJ*, 662, 1136
- Dastidar R., et al., 2018, *MNRAS*, 479, 2421
- Dessart L., Hillier D. J., 2005, *A&A*, 439, 671
- Dessart L., Hillier D. J., 2019, *A&A*, 625, A9
- Dessart L., Hillier D. J., Waldman R., Livne E., 2013, *MNRAS*, 433, 1745
- Dessart L., et al., 2014, *MNRAS*, 440, 1856
- Dhungana G., et al., 2016, *ApJ*, 822, 6
- Falk S. W., Arnett W. D., 1977, *ApJS*, 33, 515
- Faran T., et al., 2014, *MNRAS*, 445, 554
- Faran T., Nakar E., Poznanski D., 2018, *MNRAS*, 473, 513
- Gall E. E. E., et al., 2015, *A&A*, 582, A3
- González-Gaitán S., et al., 2015, *MNRAS*, 451, 2212
- Grassberg E. K., Imshennik V. S., Nadyozhin D. K., 1971, *Ap&SS*, 10, 28
- Gutiérrez C. P., et al., 2017a, *ApJ*, 850, 89
- Gutiérrez C. P., et al., 2017b, *ApJ*, 850, 90
- Hamuy M., 2003, *ApJ*, 582, 905
- Hamuy M., Suntzeff N. B., 1990, *AJ*, 99, 1146
- Hamuy M., et al., 2001, *ApJ*, 558, 615
- Henry R. B. C., Worthey G., 1999, *PASP*, 111, 919
- Hosseinzadeh G., Valenti S., Arcavi I., Howell D. A., McCully C., 2015, *The Astronomer's Telegram*, 8102
- Huang F., et al., 2015, *ApJ*, 807, 59
- Inserra C., et al., 2012, *MNRAS*, 422, 1122
- Jordi K., Grebel E. K., Ammon K., 2006, *A&A*, 460, 339
- Leonard D. C., et al., 2002, *PASP*, 114, 35
- Lusk J. A., Baron E., 2017, *PASP*, 129, 044202
- Makarov D., Prugniel P., Terekhova N., Courtois H., Vauglin I., 2014, *A&A*, 570, A13
- Minkowski R., 1941, *PASP*, 53, 224
- Moriya T. J., Tominaga N., 2012, *ApJ*, 747, 118
- Morozova V., Piro A. L., Valenti S., 2017, *ApJ*, 838, 28
- Morozova V., Piro A. L., Valenti S., 2018, *ApJ*, 858, 15
- Nagy A. P., 2018, *ApJ*, 862, 143
- Nagy A. P., Vinkó J., 2016, *A&A*, 589, A53
- Nagy A. P., Ordasi A., Vinkó J., Wheeler J. C., 2014, *A&A*, 571, A77
- Nugent P., et al., 2006, *ApJ*, 645, 841
- Pastorello A., et al., 2006, *MNRAS*, 370, 1752
- Pastorello A., et al., 2009, *MNRAS*, 394, 2266
- Patat F., Barbon R., Cappellaro E., Turatto M., 1994, *A&A*, 282, 731
- Polshaw J., et al., 2015, *A&A*, 580, L15
- Polshaw J., et al., 2016, *A&A*, 588, A1
- Poznanski D., Prochaska J. X., Bloom J. S., 2012, *MNRAS*, 426, 1465
- Pumo M. L., Zampieri L., Spiro S., Pastorello A., Benetti S., Cappellaro E., Manicò G., Turatto M., 2017, *MNRAS*, 464, 3013
- Riess A. G., et al., 2018, *ApJ*, 855, 136
- Sanders N. E., et al., 2015, *ApJ*, 799, 208
- Schlafly E. F., Finkbeiner D. P., 2011, *ApJ*, 737, 103
- Singh A., Srivastav S., Kumar B., Anupama G. C., Sahu D. K., 2018, *MNRAS*, 480, 2475
- Smartt S. J., 2015, *Publ. Astron. Soc. Australia*, 32, e016
- Smartt S. J., Eldridge J. J., Crockett R. M., Maund J. R., 2009, *MNRAS*, 395, 1409
- Spiro S., et al., 2014, *MNRAS*, 439, 2873
- Stetson P. B., 1987, *PASP*, 99, 191
- Szalai T., et al., 2019, *ApJ*, 876, 19
- Takáts K., et al., 2014, *MNRAS*, 438, 368
- Theureau G., Bottinelli L., Coudreau-Durand N., Gouguenheim L., Hallet N., Loulergue M., Paturel G., Teerikorpi P., 1998, *A&AS*, 130, 333
- Thomas R. C., Nugent P. E., Meza J. C., 2011, *PASP*, 123, 237
- Utrobin V. P., Chugai N. N., 2013, *A&A*, 555, A145
- Valenti S., et al., 2015, *MNRAS*, 448, 2608
- Valenti S., et al., 2016, *MNRAS*, 459, 3939
- Yuan F., et al., 2016, *MNRAS*, 461, 2003
- de Jaeger T., et al., 2018, *MNRAS*, 476, 4592
- van Dokkum P. G., 2001, *PASP*, 113, 1420

This paper has been typeset from a  $\text{\TeX}/\text{\LaTeX}$  file prepared by the author.